



Cite this: *Nanoscale*, 2017, 9, 10701

Diruthenium(II,III) metallodrugs of ibuprofen and naproxen encapsulated in intravenously injectable polymer–lipid nanoparticles exhibit enhanced activity against breast and prostate cancer cells†

Samara R. Alves Rico, ^{a,b} Azhar Z. Abbasi, ^{‡,b} Geise Ribeiro,^{§a} Taksim Ahmed, ^b Xiao Yu Wu ^{*b} and Denise de Oliveira Silva ^{*a}

A unique class of diruthenium(II,III) metallodrugs containing non-steroidal anti-inflammatory drug (NSAID), Ru₂(NSAID), have been reported to show anticancer activity in glioma models *in vitro* and *in vivo*. This work reports the encapsulation of the lead metallodrug of ibuprofen (Hlbp), [Ru₂(lbp)₄Cl] or Ru₂lbp, and also of the new analogue of naproxen (HNpx), [Ru₂(Npx)₄Cl] or Ru₂Npx, in novel intravenously (*i.v.*) injectable solid polymer–lipid nanoparticles (SPLNs). A rationally selected composition of lipids/polymers rendered nearly spherical Ru₂(NSAID)-SPLNs with a mean size of 120 nm and zeta potential of about –20 mV. The Ru₂(NSAID)-SPLNs are characterized by spectroscopic techniques and the composition in terms of ruthenium–drug species is analyzed by mass spectrometry. The metallodrug-loaded nanoparticles showed high drug loading (17–18%) with ~100% drug loading efficiency, and good colloidal stability in serum at body temperature. Fluorescence-labeled SPLNs were taken up by the cancer cells in a time- and energy-dependent manner as analyzed by confocal microscopy and fluorescence spectrometry. The Ru₂(NSAID)-SPLNs showed enhanced cytotoxicity (IC₅₀ at 60–100 μmol L^{–1}) in relation to the corresponding Ru₂(NSAID) metallodrugs in breast (EMT6 and MDA-MB-231) and prostate (DU145) cancer cells *in vitro*. The cell viability of both metallodrug nanoformulations is also compared with those of the parent NSAIDs, Hlbp and HNpx, and their corresponding NSAID-SPLNs. *In vivo* and *ex vivo* fluorescence imaging revealed good biodistribution and high tumor accumulation of fluorescence-labeled SPLNs following *i.v.* injection in an orthotopic breast tumor model. The enhanced anticancer activity of the metallodrug-loaded SPLNs in these cell lines can be associated with the advantages of the nanoformulations, assigned mainly to the stability of the colloidal nanoparticles suitable for *i.v.* injection and enhanced cellular uptake. The findings of this work encourage future *in vivo* efficacy studies to further exploit the potential of the novel Ru₂(NSAID)-SPLN nanoformulations for clinical application.

Received 4th March 2017,

Accepted 12th June 2017

DOI: 10.1039/c7nr01582h

rs.c.li/nanoscale

^aLaboratory for Synthetic and Structural Inorganic Chemistry - Bioinorganic and Metallodrugs, Department of Fundamental Chemistry, Institute of Chemistry, University of São Paulo, Av. Prof. Lineu Prestes, 748, B2 T, 05508-000 São Paulo, SP, Brazil. E-mail: deosilva@iq.usp.br; Tel: +55(11)30919124

^bAdvanced Pharmaceutics and Drug Delivery Laboratory, Leslie Dan Faculty of Pharmacy, University of Toronto, Toronto, ON, M5S 3M2, Canada. E-mail: xywu@phm.utoronto.ca

† Electronic supplementary information (ESI) available: Cell uptake fluorescence microscopy images and CSLM of SPLNs in EMT6, MDA-MB-231 and DU145 cancer cell lines. See DOI: 10.1039/c7nr01582h

‡ Present address: Product Life Cycle Management (R&D) Department, Apotex Inc. 150 Signet Dr, North York, ON M9L 1T9, Canada.

§ Present address: Physics and Chemistry Institute, Federal University of Itajubá, Av BPS 1303, 37500-903, Itajubá, MG, Brazil.

1. Introduction

Cancer is a major cause of death in the world and a complex disease that requires multiple therapeutic approaches including chemotherapy alongside with other treatments. Platinum-based anticancer drugs are commonly used for chemotherapy; however their benefit is limited by the problems of drug resistance and severe systemic toxicity.¹ A number of formulation strategies for targeting and delivery of the clinic used platinum anticancer drugs aiming to enhance efficacy and reduce adverse effects among other features, has been reviewed.² A promising formulation of cisplatin–lipid nanoparticles (NPs) has reached Phase III clinical trials.³ Non-platinum-based anticancer drugs have also attracted attention in the last few years, pointing to the ruthenium compounds as a great promise for

the next generation of metallo-anticancer drugs. A number of Ru(II) and Ru(III) antitumor compounds have been developed over the past two decades.^{4–8} However, few of them have reached pre-clinical evaluation with only two Ru(III)-drugs entering clinical trials – the anti-metastatic (Him) $[\text{RuCl}_4(\text{dmsO})(\text{im})]$, im = 1-*H*-imidazole, NAMI-A,^{9,10} and the cytotoxic $[\text{RuCl}_4(\text{ind})_2]$, ind = 1-*H*-indazole, X = Hind⁺, KP1019¹¹ or Na⁺, NKP1339.¹² A unique class of diruthenium metallodrugs has been synthesized in de Oliveira Silva's laboratory by coordinating the mixed-valence Ru₂(II,III) metal-metal bonded core to carboxylates derived from bioactive ligands, such as the γ -linolenic acid^{13,14} and non-steroidal anti-inflammatory drugs (NSAIDs).^{15–20} The NSAID ligands, aside the anti-inflammatory properties, were shown to reduce significantly the risk of tumor malignancies, such as colorectal, esophagus, stomach, skin, breast, lung, prostate and urinary bladder cancer,²¹ in long-term use. The regular intake of ibuprofen was chemopreventive for breast cancer.²² The NSAIDs were also capable of inhibiting cell proliferation and inducing apoptosis in several types of cancer cells. The mode of action, although not well established yet, might be partially associated with either the inhibition of the activity of cyclooxygenase isoforms (COX-1 or COX-2) or a COX independent mechanism.^{23,24}

The Ru₂(NSAID) metallodrugs contain four equatorial drug ligands in the $[\text{Ru}_2(\text{O}_2\text{CR})_4]$ paddlewheel structured unit, while anionic or neutral ligands occupy the axial sites.^{4,5} The $[\text{Ru}_2(\text{Ibp})_4\text{Cl}]$, RuIbp, Ibp = anion from ibuprofen, exhibited anti-inflammatory activity similar to that of ibuprofen (HIbp), whereas gastrointestinal ulcerative effects were significantly reduced by the coordination of the drug to the dimetallic center in relation to the parent organic drug.¹⁵ This compound (RuIbp) and the $[\text{Ru}_2(\text{Npx})_4(\text{H}_2\text{O})_2]\text{PF}_6$, Npx = anion from naproxen (aqua-RuNpx), were capable of inhibiting proliferation of C6 rat glioma cells. The enhanced antitumor activity in relation to the corresponding NSAIDs suggested synergistic effects between the metal and the drug.¹⁶ The RuIbp metallodrug may have multiple targets, involving important proteins (p21, p27, p53, Bax, and COX-1), as shown by its effects on the C6 cell cycle.¹⁷ *In vivo* studies revealed the efficacy of RuIbp in decreasing tumor area in C6 rat orthotopic glioma model, and the low toxicity of the drug in normal Wistar rats.¹⁸ The RuIbp also inhibited the proliferation of human glioma cells *in vitro*. Studies with different types of cells, *i.e.*, U87MG and A172 (p53 wild type), U138MG and U251MG (p53 mutant type) suggested that p53 and COX-1 may play a key role in the mode of action of RuIbp since the p53 mutant U138MG showed low sensitivity to the drug.¹⁸ RuIbp and axially-modified analogues¹⁹ were shown to inhibit proliferation, increase apoptosis, and inhibit mitosis and cell migration *in vitro* in U87MG and A172 cells, opening prospective routes to reach major chemotherapeutic targets in high grade gliomas. Despite the promising anticancer activity in a malignant glioma model, RuIbp and aqua-RuNpx weakly affected the proliferation of human colon carcinoma cells (HT-29 and Caco-2)²⁰ and showed no significant effects on Hep2 human larynx or T24/

83 human bladder tumor.¹⁶ The mechanism of action of the Ru₂-metallodrugs is still under investigation, however it is already known that the $[\text{Ru}_2(\text{O}_2\text{CR})_4]$ paddlewheel unit may interact with potential biological targets.^{25–30}

The major limitation for clinical use of the anticancer Ru₂(NSAID) metallodrugs, however, might be the poor water-solubility which could make them unsuited for intravenous (i.v.) administration. To overcome this problem, in this work, we propose to encapsulate the Ru₂(NSAID) metallodrugs in solid polymer-lipid nanoparticles (SPLNs). SPLNs are emerging nanocarrier systems made of hybrid building blocks of polymers and lipids initially developed by Wu and co-workers.^{31–34} With rationally selected formulations, SPLNs can accommodate a variety of payloads^{31–33} including poorly soluble drugs,³⁴ metal ions,³⁵ metal oxides,^{36,37} and quantum dots.^{38–41} SPLNs with proper size and surface properties, like other nanocarrier systems, are able to increase therapeutic efficacy and reduce adverse effects of drugs by delivering the drugs to tumors *via* the enhanced permeability and retention (EPR) effect.^{3,31–33,36,37,42–46} It has also been reported that SPLNs can bypass efflux-transporters, such as P-glycoprotein, related to multidrug resistance (MDR), consequently enhancing intracellular drug uptake and cytotoxicity of the drugs.^{43–45,47–49} In addition, the lipid or lipid-polymer core of the NPs might protect the metallodrugs thus increasing their stability, as it has been demonstrated by encapsulating the KP1019 drug in polymer micelles.⁵⁰

The present work reports novel colloiddally stable NP systems in which anticancer Ru₂(NSAID) metallodrugs (Ru₂-ibuprofen, RuIbp, or the new analogue Ru₂-naproxen, RuNpx) are encapsulated in i.v. injectable SPLNs. The cytotoxicity of the Ru₂(NSAID)-loaded SPLNs are evaluated in murine EMT6 and human MDA-MB-231 breast cancer cell lines, and also in human DU145 prostate cancer cells *in vitro*. The cell viability data of these NP systems are compared with those of the Ru₂(NSAID) metallodrugs, parent NSAIDs, ibuprofen (HIbp) and naproxen (HNpx), and their corresponding NSAID-SPLNs, and a non-drug diruthenium compound. Cellular uptake assays and *in vivo* and *ex vivo* fluorescence imaging in an orthotopic breast tumor model following i.v. injection have been performed for fluorescence-labeled SPLNs.

2. Materials and methods

2.1. Materials

All chemicals were of analytical reagent grade. Ibuprofen (HIbp, Natural Pharma) and naproxen (HNpx, Purifarma) were purchased from manipulation pharmacies in São Paulo, Brazil. RuIbp was synthesized from $[\text{Ru}_2(\text{O}_2\text{CCH}_3)_4\text{Cl}]$, RuAc, according to previously described procedures.^{19,27} Ru(III) chloride was from Sigma-Aldrich (Brazil), and solvents from Merck or LabSynth (Brazil). Myristic acid (MyA), polyoxyethylene (100) stearate (Stearate-PEG 100), polyoxyethylene (40) stearate (Stearate-PEG 40), thiazolyl blue tetrazolium bromide (MTT), polyvinyl alcohol (PVA), Nile red (a fluorescent dye), and sol-

vents used in the anhydrous form were purchased from Sigma-Aldrich (Canada). Polysorbate 80 (PS80) was from Croda (Canada), arachidic acid ethyl ester (ethyl arachidate, EA ester) from Tokyo Kasei (Japan), and cell nucleus staining dye Hoeschst 33342 from Life Technologies (Canada). Water in all experiments was distilled deionized (DDI).

2.2. Synthesis and characterization of the diruthenium(*n,m*)-naproxen compound

2.2.1. Synthesis of [Ru₂(Npx)₄Cl], RuNpx. Solutions of RuAc (0.31 g, 0.66 mmol, 50 mL water, obtained after reducing in a rotary-evaporator the initial volume of 200 mL previously stirred for 30 min), HNpx (0.76 g, 3.31 mmol, 80 mL ethanol) and LiCl (0.32 g, 5.0 mL water) were mixed and stirred under nitrogen at about 60 °C for 2 h. The mixture was filtered, and the brown solid was washed with water and a few drops of ethanol. The product was dried in a vacuum desiccator over phosphorus pentoxide and silica gel. RuNpx (0.55 g, 71%). Anal. calc. (%) found: C, 56.22; H, 4.56 and C₅₆H₅₂O₁₂ClRu₂·2 H₂O requires C, 56.49; H, 4.74. Electrospray Ionization Mass Spectrometry, ESI-MS(+) in MeOH: (*m/z*): 1120.15, [Ru₂(C₁₄H₁₃O₃)₄]⁺ requires 1120.15. Molar conductivity/S cm² mol⁻¹ (acetonitrile): 3.2. Magnetic moment, μ_{eff}/B. M.: 4.4. UV/VIS/NIR, λ/nm (ε/dm³ mol⁻¹ cm⁻¹): 480(-), 1130(-) solid; 432 (975) ethanol; 453 (1300) chloroform. Fourier Transformed Infrared, FTIR, major bands/cm⁻¹: ν 3055–2830 (CH); ν 1632 (CC)_{ring}; ν 1604 (def CH); ν 1506 (CC)_{ring}; ν_a 1458 (COO); ν_s 1407 (COO); δ 1366 (CH₃); ν 1271 (C_{ring}-O-C); ν 1070, 1026, (C-O_{ether}-C); ν 480 (Ru-O). Raman band/cm⁻¹: ν 350 (Ru-Ru). Thermogravimetry analysis, TGA, temperature range/°C (total mass loss/%): 25–400 (77.7).

2.2.2. Instrumentation and sample preparation for characterization of RuNpx. Elemental analysis (C, H) was performed on a PerkinElmer CHN 2400 elemental analyzer, at the Analytical Center of the Institute of Chemistry, University of São Paulo. The ESI-MS spectrum of RuNpx (dissolved in 1 : 1 (v/v) methanol : aqueous 0.1% formic acid) was acquired on an Agilent 6538 UHD equipment, at the Mass Spectrometry Laboratory, University of Toronto. All the other experiments were performed at the Institute of Chemistry, University of São Paulo. The conductivity of 1 × 10⁻³ mol L⁻¹ RuNpx in acetonitrile was measured on a Digimed DM-31 equipment at 25.0 ± 0.5 °C (KCl aqueous solution 146.9 μS cm⁻¹ at 25.0 °C, cell constant 0.1 cm⁻¹, was used for calibration). The magnetic susceptibility was measured by the Faraday method on powdered samples at room temperature using a Cahn DTL 7500 electrobalance (diamagnetic corrections were made by Pascal's constants, and Hg[Co(SCN)₄] was the standard). Electronic absorption spectra of the compound in solution were recorded on a Shimadzu UV-1650 PC spectrophotometer, and the solid reflectance spectrum was recorded on a Guided Wave-260 spectrophotometer equipped with optical fiber. FTIR spectrum of the solid dispersed in KBr (4000–400 cm⁻¹) was recorded on an ABB Bomen MB-102 spectrophotometer coupled to a diffuse reflectance accessory (Pike Technologies Inc.). The Raman spectrum of the solid RuNpx was recorded on a micro-

Raman Renishaw System 3000 (laser line, 632.8 nm). The TGA was conducted on a TGA-50 Shimadzu thermobalance (~5 mg sample; platinum crucible; synthetic air atmosphere; 25–1000 °C; 50 mL min⁻¹; 10 °C min⁻¹).

2.3. Preparation and characterization of the SPLNs

2.3.1. Preparation of the loaded and non-loaded SPLNs. The loaded-SPLNs were prepared from an oil-in-water emulsion followed by solvent evaporation, according to a procedure previously reported with some modifications.³⁶ An aqueous solution of 0.5 wt% PVA (100 μL) was diluted with water (600 μL) in a 5 mL eppendorf tube which was immersed into a water-bath at 64 °C (a). In parallel, two other solutions were prepared in 1.5 mL eppendorf tubes: the first one containing the drug (*i.e.*, RuIbp (2.8 mg), RuNpx (3.0 mg), HIbp (2.1 mg) or HNpx (2.4 mg)) and MyA (3 mg) dissolved in chloroform (100 μL) (b), and the second one containing EA ester (7 mg), stearate-PEG 40 (1 mg) and stearate-PEG 100 (2 mg) in chloroform (50 μL) (c). Solution (b) was added to (a) under sonication (ultrasonic processor, 100 Hz, 5 mm probe depth). After that, solution (c) was immediately added, and the resulting mixture was sonicated for 3 min (under the same conditions). The final emulsion was added quickly to ice-cold DDI water (300 μL) that was in an ice-bath and the system was maintained in the ice-bath for 5 min. After that, the emulsion was subjected to vacuum in a vacuum chamber for 10 min. The suspension of the loaded-SPLNs was stored at 4 °C. A similar procedure, but without the drug, was used to prepare a drug free formulation (non-loaded blank-SPLNs). Fluorescent NPs for cell uptake studies were prepared by the same procedure used for blank-SPLNs, but in the presence of 20 μL of Nile red chloroform solution (5 mg mL⁻¹). Fluorescent NPs for bio-distribution studies were prepared by a similar procedure used for blank-SPLNs, but in the presence of 30 μL of a 20 mg mL⁻¹ methanol solution of indocyanine green dye (ICG from MP Biomedicals, USA). A schematic diagram of the preparation of the Ru₂(NSAID)-SPLNs is shown in Fig. 1.

2.3.2. Instrumentation and sample preparation for characterization of SPLNs. To observe the morphology of NPs, a drop of the SPLNs suspension diluted in DDI water was placed on a carbon-coated grid, and allowed to dry at room temperature. The image was recorded by transmission electron microscopy (TEM) on a Hitachi H7000 microscope using an accelerating voltage of 100 kV. The size distribution and surface charge of the SPLNs were measured using the Malvern zeta sizer Nano-ZS. The stability of the SPLNs in a growth medium (see composition in the next section) was evaluated by observing the change in particle size up to 72 h at 37 °C. The electronic absorption spectra were recorded on a Cary 8454 spectrophotometer, Agilent Technologies. In a typical experiment for drug loading, 1.0 mL of SPLNs was centrifuged through a 30 kDa Amicon® filter, at 4400 rpm for 15 min, then the supernatant was diluted to 3.0 mL with ethanol : water (50 : 50 v/v). Calibration curves were built for the Ru₂(NSAID) metallodrugs and the corresponding NSAIDs in ethanol : water (50 : 50 v/v) at λ/nm: 432 (RuIbp), 264 (HIbp), 316 (RuNpx), and 317 (HNpx).

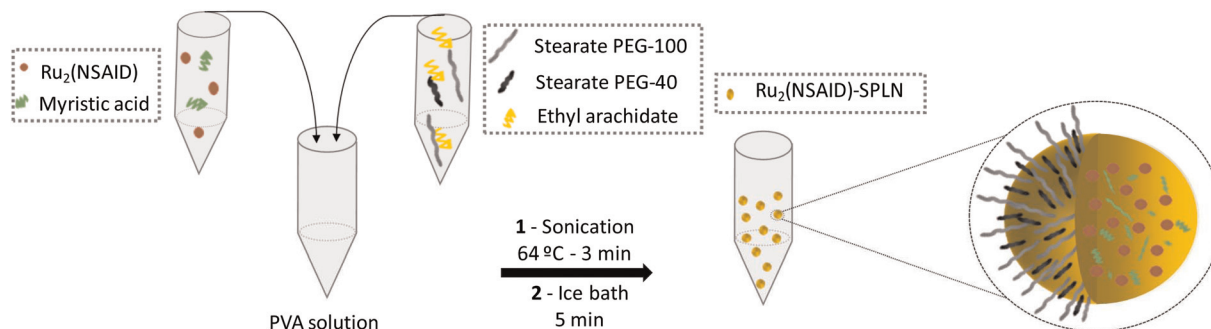


Fig. 1 Schematic diagram representing the preparation of Ru₂(NSAID)-SPLN formulations.

The electronic spectra of Ru₂(NSAID) metallodrugs were recorded for ethanolic solutions of the Ru₂(NSAID)-SPLNs retained in 30 kDa Amicon® filters after centrifugation at 4400 rpm for 15 min. The ESI-MS spectra were recorded for Ru₂(NSAID)-SPLNs on a Bruker Daltonics Micro TOF equipment (NPs dissolved in methanol) at the Analytical Center of Institute of Chemistry, University of São Paulo, or on an Agilent 6538 UHD equipment (NPs centrifuged solid dissolved in 1:1 (v/v) methanol : aqueous 0.1% formic acid), at the Mass Spectrometry Laboratory at University of Toronto. The FTIR spectra of Ru₂(NSAID)-SPLNs were recorded on a PerkinElmer Spectrum One equipment with an ATR accessory for solid samples after 2 h ultracentrifugation at 43 000 rpm, at the University of Toronto.

2.4. *In vitro* biological assays

2.4.1. Time-dependent cellular uptake of SPLNs. Murine EMT6 breast cancer (obtained initially from Dr I. Tannock, Ontario Cancer Institute and maintained in Dr X. Y. Wu's laboratory), human MDA-MB-231 breast cancer and DU145 prostate cancer cells (American Type Culture Collection (ATCC), USA) were cultured at a density of 3×10^4 cells per mL in a 96-well plate in growth medium (*i.e.*, alpha-minimal essential medium (α MEM), 10% fetal bovine serum (FBS) and 5% penicillin-streptomycin, all of them from Life Technologies, Canada) at 37 °C, under a 5% CO₂ atmosphere, for 24 h. Next day, medium from each well was aspirated, and 0.2 mL of fresh growth medium containing fluorescent dye labeled SPLNs (1 mg mL^{-1}) was added. Cells were incubated for 0.5, 1, 2, 3, 4, 6 and 24 h. After each time point, cells were washed twice with PBS (phosphate buffer saline) buffer, and cell fluorescence was measured with a microplate reader SpectraMAX GeminiXS (Molecular Devices) using an excitation wavelength of 540 nm and recording the fluorescence at 630 nm.

2.4.2. Temperature-dependent cellular uptake of SPLNs. Murine EMT6 breast cancer, human MDA-MB-231 breast cancer and DU145 prostate cancer cells were cultured in growth medium at a density of 1×10^5 cells per mL into two different Petri dishes, and maintained at 37 °C for 24 h (in 5% CO₂, 95% humidified air). After 24 h, one of the dishes was placed at 4 °C for 1 h, while the other remained at 37 °C. After one hour, the medium from each dish was aspirated and 2 mL

of fresh growth medium containing fluorescent dye labeled SPLNs (1 mg mL^{-1}) was added. The dishes were incubated again at 37 °C or 4 °C for another 2 h. After the required time, the cells were washed twice with PBS, and the cell nuclei were stained by incubating cells with 2 mL growth medium containing Hoechst 33342 ($0.5 \text{ } \mu\text{g mL}^{-1}$) at 37 °C for 10 min. The cells were then washed twice with growth medium, incubated again in fresh growth medium, and then, cell uptake was observed using a fluorescence microscope EVOS AMG. The quantitative difference in fluorescence intensity was also evaluated by performing the same procedure in a 96-well plate described in section 2.4.1. The only difference in the conditions is that one plate with fluorescent dye labeled SPLNs was kept at 4 °C for 3 h and another at 37 °C for 3 h.

2.4.3. Confocal fluorescence microscopic analysis. Murine EMT6 breast cancer, human MDA-MB-231 breast cancer and DU145 prostate cancer cells were cultured in growth medium at a density of 1×10^5 cells per mL in small Petri dishes made for confocal microscopy and maintained at 37 °C for 24 h in 5% CO₂. After 24 h, the medium from each dish was aspirated and replaced with 2 mL of growth medium containing fluorescent dye labeled SPLNs (1 mg mL^{-1}), and the cells were incubated at 37 °C for another 2 h. The cells were then washed twice with PBS buffer, and the cell nuclei were stained by incubation with 2 mL of growth medium containing Hoechst 33342 ($0.5 \text{ } \mu\text{g mL}^{-1}$) at 37 °C for 10 min. The cells were then washed twice with growth medium and finally incubated in growth medium. Cellular internalization of SPLNs was confirmed using a confocal laser scanning microscope (CLSM) (Zeiss LSM 510) by taking the z-stack images up to 10 μm depth using a 40 \times objective lens.

2.4.4. Determination of cell viability. *In vitro* cell viability of drugs (Hibp and HNpx), ruthenium compounds (RuAc, RuIbp and RuNpx), loaded SPLNs (Hibp-SPLNs, RuIbp-SPLNs, HNpx-SPLNs and RuNpx-SPLNs) and the biocompatibility of drug free non-loaded NPs (blank-SPLNs) were determined by MTT assay in murine EMT6 breast cancer, human MDA-MB-231 breast cancer and DU145 prostate cancer cell lines. Cells were incubated at a density of 1×10^4 cells per well in a 96-well plate at 37 °C in 5% CO₂, for 24 h. Stock solutions of compounds were prepared as follows: organic drugs, Hibp

or HNpx, 80 mmol L⁻¹ ethanol solution was diluted to 800 μmol L⁻¹ with growth medium containing PS80 (0.01%); Ru₂-NSAID compound, RuIbp or RuNpx, 20 mmol L⁻¹ ethanol solution was diluted to 200 μmol L⁻¹ with growth medium containing PS80 (0.01%) (1% ethanol in final solution), RuAc, 6.7 mmol L⁻¹ in water was diluted with growth medium. A suspension of HIbp-SPLNs or HNpx-SPLNs and 10.4 mmol L⁻¹ drug was diluted with growth medium to 800 μmol L⁻¹ drug concentration. A suspension of RuIbp-SPLNs or RuNpx-SPLNs and 2.6 mmol L⁻¹ drug was diluted with growth medium to 200 μmol L⁻¹ drug concentration. Suspensions of drug free non-loaded NPs (blank-SPLNs) were prepared by a similar procedure to their corresponding loaded-SPLNs. The stock solutions were serially diluted with growth medium to concentrations in the range 1–200 μmol L⁻¹ (Ru₂ compounds) or 4–800 μmol L⁻¹ (NSAID), then 0.2 mL was added to each well, and the cells were incubated for 48 h. After the required time, the cells were washed with PBS, 0.1 mL MTT (1 mg mL⁻¹ in growth medium) was added, and the cells were incubated again for 4 h. Then, 0.1 mL sodium dodecyl sulfate (SDS, Bioshop, Canada) was added to each well and the cells were incubated overnight. Cell viability was determined by recording the absorbance at 572 nm using the SpectraMAX GeminiXS microplate reader.

2.5. *In vivo* and *ex vivo* biodistribution of the non-loaded SPLNs

Murine breast cancer EMT6 cells (2 × 10⁶ cells in 30 μL of growth medium) were injected into the mammary fat pad of 8–12-week-old female BALB/c mice (Jackson, Canada). Tumor growth was measured using the vernier calliper. All animal experiments were performed in accordance with guidelines and regulation of the Animal Care Committee at University Health Network. Once the tumor volume reached 300–400 mm³ at about two to three weeks from the date of tumor cell implantation, 200 μL of ICG-loaded SPLNs was injected *via* the tail vein. The *in vivo* bio-distribution and tumor uptake of the SPLNs were monitored non-invasively up to 24 h using the Xenogen IVIS Spectrum Imaging System (Caliper Life Sciences Inc.). During the acquisition of images, mice were anesthetized with isoflurane. For all the images, the fluorescence intensity was equalized to quantify the SPLNs distribution in the whole body. To examine the *ex vivo* accumulation of the SPLNs, the animals were euthanized at 4 h and 24 h post blank-SPLNs injection *via* the tail vein. The tumor and selected organs (heart, lungs, liver, intestine and kidneys) were collected. *Ex vivo* fluorescence images of whole organs were recorded, and the fluorescence intensities were measured in terms of average radiant efficiency by manually drawing the same area of regions of interest (ROI).

2.6. Statistical data analysis

Data are presented as the mean ± standard deviation (SD) for results obtained from three independent trials unless otherwise indicated. Statistical significance between two groups was tested with a Student's *t* test and between three groups with

analysis of variance ANOVA. Differences were considered significant at *p* < 0.05.

3. Results and discussion

3.1. Synthesis and characterization of the diruthenium-naproxen compound, RuNpx

Two Ru₂(NSAID) metallodrugs, *i.e.*, the known RuIbp^{15,16,19} and the naproxen analogue reported for the first time, RuNpx, were selected here to be encapsulated in the SPLNs. The choice for the chlorido-RuNpx, instead of the previously reported aqua-RuNpx,^{16,20} was due to the axially coordinated halide which contributes to counterbalance the positive charge of the [Ru₂(NSAID)₄]⁺ paddlewheel unit (Fig. 2a) giving neutral species. The new RuNpx, prepared from RuAc and HNpx, was formulated as [Ru₂(Npx)₄Cl]·2H₂O with the basis on elemental analysis data, and the composition was corroborated by mass spectrometry. The ESI-MS(+) peak at maximum *m/z* 1120.15 showed typical pattern of isotopic distribution of ruthenium (see section 3.2.3), thus could be assigned to the [Ru₂(Npx)₄]⁺ fragment, in good agreement with the simulated pattern ([Ru₂(C₁₄H₁₃O₃)₄]⁺, calc. *m/z* 1120.15). Four naproxen anions are equatorially bonded to the dimetallic core while the halide occupies the axial position. Similar to RuIbp, the solid formed by neutral species has the [Ru₂(Npx)₄] paddlewheel units connected by Ru–Cl axial bridges to give polymeric chains. The low molar conductance in acetonitrile (3.2 S cm² mol⁻¹) is consistent with non-electrolyte behavior,⁵¹ thus corroborating the axial binding of the chloride to the Ru₂(II,III) core. The maintenance of the multiple bond in the metal–metal core after the equatorial ligand substitution reaction was confirmed by magnetic measurements and electronic absorption spectroscopy. The high effective magnetic moment (4.4 B.M.) of RuNpx is consistent with the Ru₂(II,III) core of bond order 2.5 and three unpaired electrons per dinuclear unit.^{19,52,53} The electronic spectrum of the solid shows a VIS band at 480 nm and a NIR band around 1130 nm, assigned predominantly to the π(Ru–O) → π*(Ru₂) and the δ(Ru₂) → δ*(Ru₂) electronic transitions, respectively.^{19,54,55} Similar to the previous findings for the RuIbp in solution,¹⁹ the energy of the VIS band of RuNpx depends on the nature of the solvent. A shift to 453 nm is observed in the non-coordinating chloroform, while the band appears at a higher energy (432 nm) in ethanol, which suggests axial substitution of chloride by coordinating solvents. The FTIR spectrum of RuNpx was quite similar to that of the aqua-RuNpx analogue,¹⁶ except for the bands associated with the axial ligand. The ν(CO) carbonyl stretching band of HNpx (1728 cm⁻¹) disappeared in the spectrum of RuNpx indicating total absence of the parent acid in the solid of the metallodrug. The deprotonation of the HNpx drug to give the corresponding carboxylate anion (Npx) was confirmed by the appearance of two new bands, at 1458 and 1407 cm⁻¹, typical of the ν_a(COO) asymmetric and ν_s(COO) symmetric stretching modes of the carboxylate, respectively.

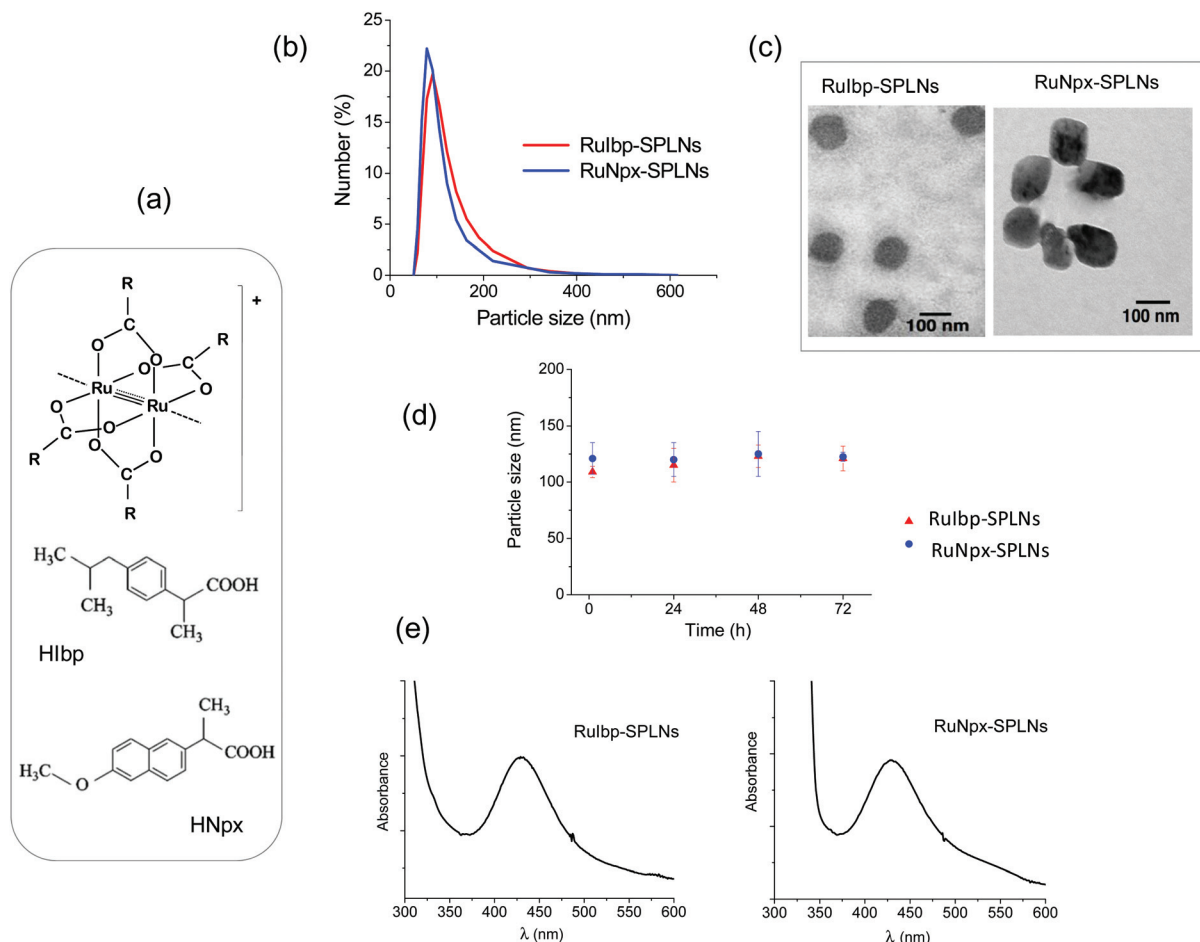


Fig. 2 (a) Paddlewheel structure of the Ru₂(NSAID) metallodrugs and structures of Hlbp and HNpx. (b) Particle size distribution of Ru₂(NSAID)-SPLNs. (c) TEM image of Ru₂(NSAID)-SPLNs (70 000 \times). (d) Particle size of Ru₂(NSAID)-SPLNs in growth medium at 37 °C as a function of time. (e) Electronic absorption spectra of Ru₂(NSAID)-SPLNs.

The small value (51 cm⁻¹) of the frequency difference between ν_a and ν_s of the $\nu(\text{COO})$ stretching modes is in agreement with the bridging coordination of the drug carboxylate group. The characteristic bands (cm⁻¹) of the Npx ligand were tentatively assigned to: 3055–2830, $\nu(\text{CH})$; 1632, 1604, $\nu(\text{CC})_{\text{ring}}$ and def (CH); 1506, $\nu(\text{CC})_{\text{ring}}$; 1366, $\delta(\text{CH}_3)$; 1271, $\nu(\text{C}_{\text{ring}}-\text{O}-\text{C})$; 1070, 1026, $\nu(\text{C}-\text{O}_{\text{ether}}-\text{C})$. The band at 480 cm⁻¹ may be assigned to the $\nu(\text{Ru}-\text{O})$ metal-carboxylate stretching band.¹⁶ The $\nu(\text{Ru}-\text{Ru})$ metal-metal stretching was assigned to the Raman band at 350 cm⁻¹. This frequency is slightly lower than the value (360 cm⁻¹) reported for the aqua-RuNpx, thus corroborating that the stronger coordinating chloride ligand in the axial site may contribute to weaken the metal-metal bond in the Ru₂ core, as was also shown for axially-modified Ru₂ compounds.¹⁹ The solid of RuNpx was found to be thermally stable up to 240 °C. The first step of mass loss (2.8%), below 240 °C, was consistent with the release of two water molecules. Above this temperature and up to 400 °C, the compound undergoes thermal degradation and loses 74.9% mass. This percentage of weight loss is in agreement with the dissociation of all the Npx ligands (except for four O atoms) and the chlor-

ide [calc. 74.6%, for 4 Npx + Cl - 4O], similar to the thermal degradation of the Ru₂ analogue.¹⁹ The final mass (22.3%) was in accordance with the formation of RuO₂ (2 mol, calc. 22.3%) as the thermal residue.

3.2. Preparation and characterization of the SPLNs

3.2.1. Synthesis, particle size and zeta potential. The first attempted procedure to prepare nanoformulations by encapsulating the Ru₂(NSAID) metallodrugs followed a method reported for a formulation based on the pharmaceutically acceptable myristic acid (MyA, C₁₄H₂₈O₂) lipid.³⁷ The average size (~300 nm) of the obtained NPs, however, was above the size range (<200 nm) expected to promote the EPR effect and avoid accumulation in liver and spleen.⁴² In a second attempt, to try to decrease NP size, the MyA was replaced by lipid ethyl arachidate ester (EA ester, C₂₂H₄₄O₂), which previously succeeded in producing other types of lipid NPs.⁴⁴ By using only the EA ester, smaller sized (~120 nm) NPs were produced; however, these NPs showed positive zeta potential values (+30 mV) which were considered to be not suitable for i.v. injections (due to strong binding affinity with negatively

charged proteins and cells^{36,56}). In the following experiments, a set of different combinations of both lipids was investigated until reaching the MyA:EA ratio of 3:7 w/w, which was considered the most appropriate to give metallodrug loaded-SPLNs formulations with the ideal particle size and surface charge. The experiments suggested that the more hydrophobic EA ester lipid may contribute to decrease particle size while MyA may play a key role to decrease surface charge. The presence of EA ester, in general, might also favor high loading of water-insoluble drugs. The SPLNs loaded with the organic parent NSAIDs Hlbp (Hlbp-SPLNs) and HNpx (HNpx-SPLNs), as well as drug-free blank-SPLNs (without drug) and fluorescence-labeled SPLNs (having a fluorescent dye instead of drug) were prepared by using the same ratio of both lipids. The parameters determined for the loaded-SPLNs and blank-SPLNs are shown in Table 1. Taking into account the standard deviations of the measurements, it is possible to consider that the difference in the values of particle size (mean diameter, nm) of Ru₂(NSAID)-SPLNs (*i.e.*, 120 ± 15 (RuIbp-SPLNs); 121 ± 12 (RuNpx-SPLNs)), NSAID-SPLNs (145 ± 11 (Hlbp-SPLNs); 136 ± 28 (HNpx-SPLNs)) and blank-SPLNs (130 ± 5) is not significantly different. A discussion of this phenomenon would not be trivial since the size may depend on the structural arrangement of the NPs multiple components, which can change in the presence or absence of the drugs. The polydispersity indexes (related to particle size distribution) were all in the range 0.2–0.4, in good agreement with data previously reported for other polymer–lipid NPs.⁴⁴ The mean diameter values from TEM analysis of the Ru₂(NSAID)-SPLNs corroborate the particle sizes of these NPs. Additionally, TEM images (Fig. 2c) revealed a nearly spherical shape for both metallodrug loaded-SPLNs. Moreover, the Ru₂(NSAID)-SPLNs were shown to have good colloidal stability in serum at body temperature, since no significant changes were observed in the NPs particle size kept in growth medium at 37 °C up to 3 days (Fig. 2d). The values of the zeta potential of the NP formulations were all negative (around –17 to –24 mV for the drug-loaded SPLNs and –32 mV for the blank-SPLNs).

3.2.2. Drug loading of the SPLNs. The drug content and the encapsulating efficiency of the loaded-SPLNs were determined by UV-VIS spectroscopy, as described in the Materials and methods part. The data presented in Table 1 show 14–18% drug loading, indicating that these nanoformulation systems are capable of carrying a large amount of these drugs. The encapsulation efficiency was very close to 100% for all the loaded systems, showing that the experimental procedure suc-

ceeded in encapsulating the drugs and the metallodrugs into the SPLNs.

3.2.3. Characterization of the Ru₂(NSAID)-SPLNs. The electronic absorption spectra (Fig. 2e) of ethanol solutions of the Ru₂(NSAID)-SPLNs show a visible band at about 430 nm, that is characteristic of Ru₂(II,III) tetracarboxylates having the [Ru₂(O₂CR)₄] paddlewheel structure. The identification of the diruthenium–drug species encapsulated into the loaded-SPLNs was made by mass spectra analyses. Two types of samples were investigated and both of them (the NPs directly dissolved in methanol, and the NP centrifuged solids dissolved in methanol:aqueous 0.1% formic acid) showed a similar ESI-MS(+) spectrum pattern, which is discussed here. The ESI-MS(+) spectrum of RuIbp-SPLNs (Fig. 3) shows four sets of peaks all having the typical pattern of isotopic distribution of ruthenium. The first set of peaks with maximum *m/z* 1024.28 is assigned to the [Ru₂(Ibp)₄]⁺ ionic fragment, in full agreement with the simulated MS pattern ([Ru₂(C₁₃H₁₇O₂)₄]⁺, calc. *m/z*, 1024.28) and also with the reported ESI-MS spectrum of RuIbp.¹⁹ The other three sets of peaks could be assigned to mixed species having the general formula [Ru₂(Ibp)_{4–x}(My)_x]⁺, in which the myristate (My, C₁₄H₂₇O₂[–]) partially and sequentially replaces the ibuprofenate (C₁₃H₁₇O₂[–]) anions. The assignment of the [Ru₂(Ibp)_{4–x}(My)_x]⁺ fragments in Fig. 3 is in accordance with the corresponding simulated MS pattern for the three species, *i.e.*, [Ru₂(Ibp)₃(My)₁]⁺, calc. 1046.37; [Ru₂(Ibp)₂(My)₂]⁺, calc. 1068.45; and [Ru₂(Ibp)₁(My)₃]⁺, calc. 1090.53. The ESI-MS(+) spectrum of the RuNpx-SPLNs (Fig. 3) was more difficult to interpret since, due to the close molar mass values of Npx and My, a number of superimposed peaks were observed. However, a more detailed inspection revealed that, similar to the RuIbp-SPLNs, the RuNpx-SPLNs also exhibit four sets of peaks with the typical pattern of isotopic distribution of ruthenium. The set of peaks with maximum *m/z* at 1120.15 is assigned to the [Ru₂(Npx)₄]⁺ ionic fragment, in good agreement with the ESI-MS data described in section 3.1. The other three sets of peaks could be ascribed to mixed species in which the My (C₁₄H₂₇O₂[–]) replaces the Npx (C₁₄H₁₃O₃[–]) anions. The assignment of the [Ru₂(Npx)_{4–x}(My)_x]⁺ fragments in Fig. 3 is also in accordance with the corresponding simulated MS pattern for all species, *i.e.*, [Ru₂(Npx)₃(My)₁]⁺, calc. 1118.28; [Ru₂(Npx)₂(My)₂]⁺, calc. 1116.38; and [Ru₂(Npx)₁(My)₃]⁺, calc. 1114.48. It is worth noting that the ESI-MS experiment was performed in duplicate for each of two distinct batches of synthesis, and also for two differently prepared samples, giving reproducible data regard-

Table 1 Particle size, zeta potential, polydispersity index, drug loading and encapsulation efficiency of the loaded- and non-loaded-SPLNs. Data are presented as mean ± standard deviation (*n* = 3)

NP system	Particle size (nm)	Zeta potential (mV)	Polydispersity index	Drug loading (%)	Encapsulation efficiency (%)
RuIbp-SPLNs	120 ± 15	–24.2 ± 0.98	0.300 ± 0.101	17	98
RuNpx-SPLNs	121 ± 12	–21.8 ± 0.50	0.381 ± 0.015	18	97
Hlbp-SPLNs	145 ± 11	–19.5 ± 0.53	0.260 ± 0.023	14	99
HNpx-SPLNs	136 ± 28	–17.5 ± 0.65	0.263 ± 0.024	15	98
Blank-SPLNs	130 ± 5	–32.3 ± 0.95	0.337 ± 0.041	—	—

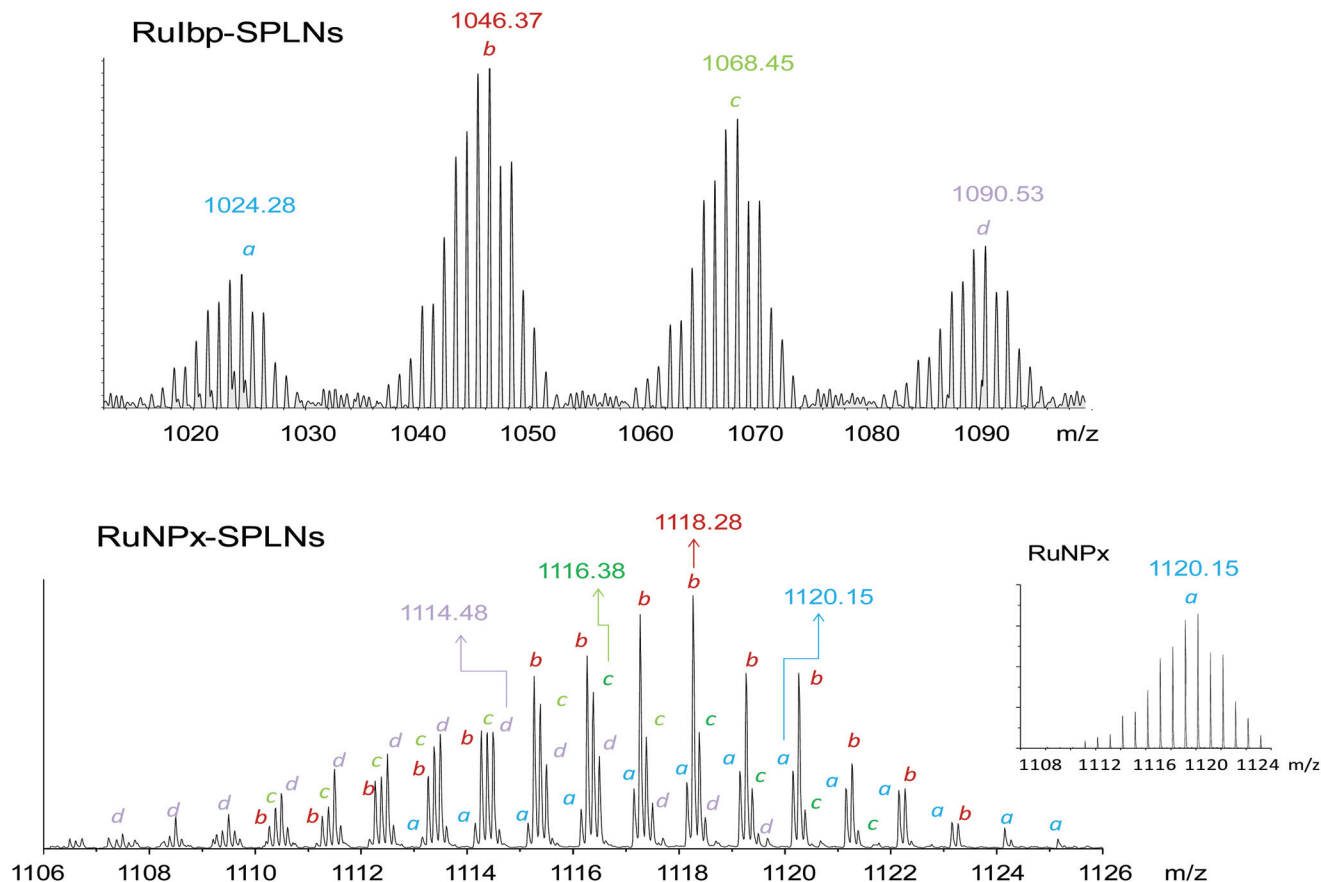


Fig. 3 ESI-MS(+) of RuIbp-SPLNs and RuNpx-SPLNs (inset, ESI-MS(+) of RuNpx). $[\text{Ru}_2(\text{NSAID})_{4-x}(\text{My})_x]^+$ fragments are represented by (a): $[\text{Ru}_2(\text{NSAID})_4]^+$; (b): $[\text{Ru}_2(\text{NSAID})_3(\text{My})_1]^+$; (c): $[\text{Ru}_2(\text{NSAID})_2(\text{My})_2]^+$; (d): $[\text{Ru}_2(\text{NSAID})_1(\text{My})_3]^+$.

ing the presence of diruthenium–drug–My mixed-species. Therefore, it is plausible to suggest that the equatorial ligand exchange may occur during the preparation of the metallodrug loaded-SPLNs. Interestingly, the $[\text{Ru}_2(\text{O}_2\text{CR})_4]$ paddlewheel structure is not broken in the process, and all of the drug–My species carry the NSAID drug anions, although in different drug:My molar ratios. It is also worth mentioning that these findings might point to a key role of the MyA in stabilizing the $\text{Ru}_2(\text{NSAID})$ -SPLN formulations. Fig. 4 shows the ATR-FTIR spectra in the region 2000–1000 cm^{-1} for the $\text{Ru}_2(\text{NSAID})$ -SPLNs, drug free blank-SPLNs and $\text{Ru}_2(\text{NSAID})$ compounds. The blank-SPLNs exhibit a strong band at 1698 accompanied by a shoulder at about 1690 cm^{-1} that may be ascribed to the $\nu(\text{C}=\text{O})$ carbonyl stretching mode,⁵⁷ giving evidence for the maintenance of the carboxylic acid form of the MyA. The bands in the region 1500–1400 cm^{-1} are related to contributions of MyA, EA ester, stearate-PEGs and PVA.⁵⁸ The spectra of the RuIbp and RuNpx metallodrugs are in agreement with the FTIR data previously reported;^{15,16,19} and presently discussed in section 3.1. The spectrum of the RuIbp-SPLNs is similar to that of the RuNpx-SPLNs, but both are significantly distinct from the spectrum of the non-drug loaded blank-SPLNs. The strong band at 1738 cm^{-1} (which is weak in the spectrum of blank-SPLNs) may be assigned mainly to the

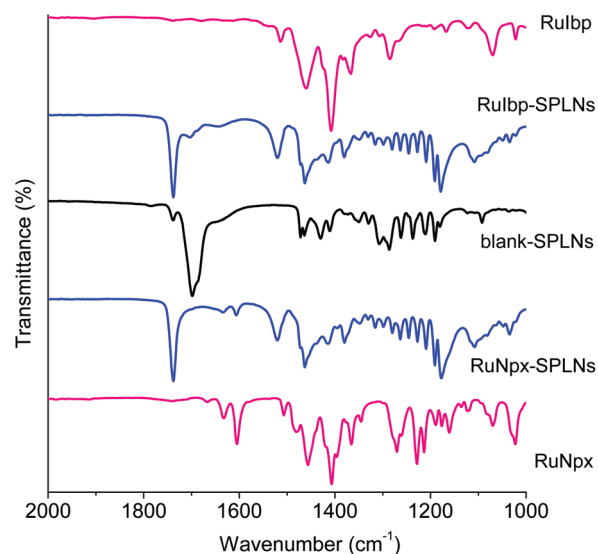


Fig. 4 ATR spectra in the region 2000–1000 cm^{-1} of RuIbp, RuIbp-SPLNs, drug free blank-SPLNs, RuNpx-SPLNs and RuNpx.

$\nu(\text{C}=\text{O})$ ester stretching mode of the EA ester, although possible contribution of the $\nu(\text{C}=\text{O})$ band of MyA less hydrogen-bonded than the fatty acid dimers⁵⁷ cannot be totally ruled out.

The presence of the $\nu(\text{C}=\text{O})$ band of the MyA seems to be not significant for both the $\text{Ru}_2(\text{NSAID})$ -SPLNs (a weak band at 1702 cm^{-1} appears for RuIbp -SPLNs, while the RuNpx -SPLNs show only the typical bands of the naproxen ligand at 1634 and 1604 cm^{-1}). Interestingly, a new band at lower frequency (1520 cm^{-1}) is observed in both $\text{Ru}_2(\text{NSAID})$ -SPLNs spectra. Ionized MyA would show a band at higher frequency ($\nu_{\text{a}}(\text{COO})$, 1550 – 1570 cm^{-1}) as has been observed for sodium myristate.^{57,59} On the other hand, a diruthenium-penta(myristate) compound was reported to show a band at 1520 cm^{-1} that was assigned to the stretching mode of the axially coordinated long-chain carboxylate.⁶⁰ Therefore, the appearance of a band at 1520 cm^{-1} in the spectra of the $\text{Ru}_2(\text{NSAID})$ -SPLNs might indicate the axial coordination of My. Then, it seems plausible to suggest that the myristic carboxylate may also interact by replacing the axial chloride ligand in the $\text{Ru}_2(\text{NSAID})$ metallogroups. The presence of free chloride in the $\text{Ru}_2(\text{NSAID})$ -SPLN suspensions was supported by adding silver nitrate, which led to the quick precipitation of silver chloride. Moreover, the pH of the $\text{Ru}_2(\text{NSAID})$ -SPLN suspensions was two units lower than the pH of the blank-SPLNs what suggests the release of protons from the deprotonation of MyA in the former systems. The ATR spectral region of 1500 – 1400 cm^{-1} is not easy to evaluate due to the band overlap of the NP multiple components, in particular the myristic and EA ester components. The $\nu(\text{COO})$ stretching modes of the NSAID carboxylate anions in the $\text{Ru}_2(\text{NSAID})$ metallogroups ($\nu_{\text{a}}(\text{COO}) \sim 1462\text{ cm}^{-1}$; $\nu_{\text{s}}(\text{COO}) \sim 1412\text{ cm}^{-1}$) should be observed in the same region for their corresponding $\text{Ru}_2(\text{NSAID})$ -SPLNs. In addition, the $\nu(\text{COO})$ vibrational mode of equatorially coordinated My, detected by ESI-MS in different mixed species, would also be expected to appear in this frequency range. These assumptions might partially explain the differences in the relative intensity of the bands of the $\text{Ru}_2(\text{NSAID})$ -SPLNs compared to the blank-SPLNs at 1500 – 1400 cm^{-1} .

3.3 In vitro cell uptake

The cell uptake of the Nile red-loaded blank-SPLNs was evaluated by time- and temperature-dependent experiments. The process was found to be time dependent for all the three investigated cell lines, EMT6, MDA-MB-231 and DU145. However, in the case of breast murine cells, a fast increase in uptake of NPs was observed in the first few hours, from 0 to about 6 h, accompanied by stabilization during this period of time (Fig. 5a). The two human cell lines, breast and prostate cells, showed slower uptake of the blank-SPLNs in the same period. To elucidate the uptake mechanism, the cells were treated and incubated at two different temperatures, $4\text{ }^\circ\text{C}$ and $37\text{ }^\circ\text{C}$. The internalization process of NPs may involve an energy-dependent mechanism, such as endocytosis process, or an energy-non-dependent mechanism, such as passive diffusion. At the lower temperature ($4\text{ }^\circ\text{C}$) the energy-dependent mechanisms are blocked since the cell membrane becomes rigid avoiding the passive diffusion process that does not need energy. The results (Fig. 5b) show a much lower (60–80% lower) cell uptake at $4\text{ }^\circ\text{C}$ than at $37\text{ }^\circ\text{C}$, suggesting that the uptake process of

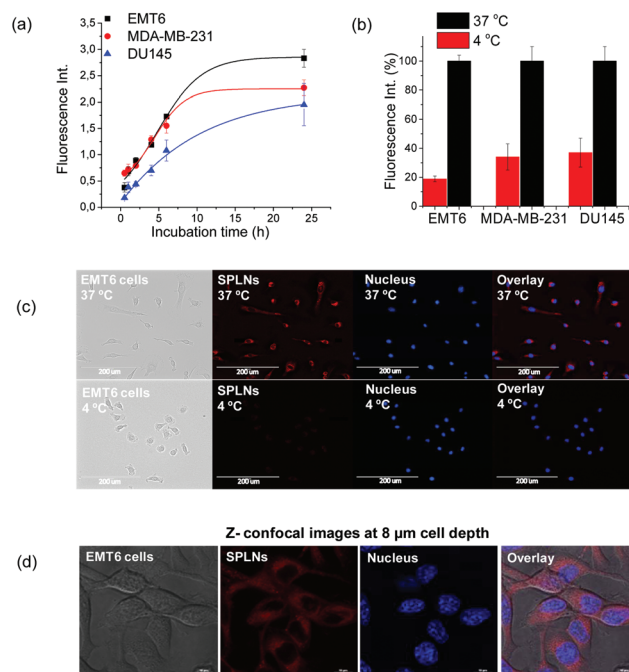


Fig. 5 (a) Fluorescence intensity as a function of incubation time (SPLNs uptake) for the three cell lines; data are presented as mean \pm standard deviation ($n = 5$). (b) Fluorescence intensity of SPLNs at $4\text{ }^\circ\text{C}$ and $37\text{ }^\circ\text{C}$; data normalized to fluorescence intensity at $37\text{ }^\circ\text{C}$ are presented as mean \pm standard deviation ($n = 5$). (c) Fluorescence microscopy images of EMT6 cells at $4\text{ }^\circ\text{C}$ and $37\text{ }^\circ\text{C}$ (2 h incubation); images from left to right are transmission light channel, red channel for Nile red labeled SPLNs, blue channel for stained nuclei and overlay of SPLNs and cell nuclei. (d) CLSM image of EMT6 illustrating the internalization of drug free SPLNs after 2 h incubation at $37\text{ }^\circ\text{C}$; the cellular uptake is visualized from overlaying images; from left to right: bright field channel, red channel for SPLN, blue channel for stained nuclei and overlay of cells, SPLN and cell nuclei; z-stack image at $8\text{ }\mu\text{m}$ depth.

blank-SPLNs is energy dependent, probably *via* endocytosis, similar to what has been observed for other polymer based NPs.^{37,61} To evaluate the intracellular location, fluorescent SPLNs were incubated with the EMT6 cells at the same temperatures, $4\text{ }^\circ\text{C}$ and $37\text{ }^\circ\text{C}$, for 3 h. The image in Fig. 5c shows the SPLNs in red and the stained nuclei in blue. At $37\text{ }^\circ\text{C}$ most of NPs were found inside the cell membrane (red fluorescence signal). The absence of SPLNs in the cell nucleus (lack of red and blue overlay) suggests that they are mostly localized in the cytoplasm. The absence of intense red signal at $4\text{ }^\circ\text{C}$ (Fig. 5c) confirms the low cell uptake in terms of fluorescence intensity at low temperature, corroborating with an energy dependent uptake mechanism. The microscope images do not allow distinguishing internalized NPs from those which might be above and/or below the cell level. The z-stack confocal scanning was then conducted to confirm that NPs are localized intracellularly, rather than just adhering on the cell surface, since the SPLNs show fluorescence only in cell depths corresponding to the internal part of the cells. The scanning from 4 to $14\text{ }\mu\text{m}$ cell depth (see the ESI†) revealed a fluorescence signal at $8\text{ }\mu\text{m}$ cell depth (Fig. 5d) that was more intense than those of the other investigated cell depths. The coexistence of a strong

intensity signal for both cell nuclei (blue) and SPLNs (red) at the same depth (8 μm) confirms that the SPLNs are localized inside the cell (specifically in the cytoplasm). Studies with MDA-MB-231 and DU145 cells showed similar results (see the ESI†), thus confirming the uptake of the SPLNs in the cytoplasm also by these two types of human cancer cell lines.

3.4. Cell viability

The effects of $\text{Ru}_2(\text{NSAID})$ -SPLN nanoformulations on the cancer cell viability were investigated *in vitro* in three different cell lines, *i.e.*, EMT6 and MDA-MB-231 breast cancer and DU145 prostate cancer cell lines. The assays were also performed for the non-drug RuAc, the free NSAIDs, HIBp and HNPx, and their corresponding loaded-SPLNs, and the drug free blank-SPLNs. The cell viability curves for all the systems compared to the control are shown in Fig. 6. The low effect of the drug free blank-SPLNs on the cell viability of all three types of cancer cells indicates good biocompatibility of the lipid NP system. Since this work is the first for testing the activity of the $\text{Ru}_2(\text{NSAID})$ metallodrugs in breast and prostate cancer cells, before discussing the behavior of the drug loaded-SPLN systems, it is interesting to compare the effects of the free metallodrugs with those of the corresponding HIBp and HNPx parent drugs, and also with that of the non-drug compound RuAc. The HIBp and HNPx free drugs were tested at the four-fold metallodrug molar concentration with the aim of maintaining the 1 Ru_2 :4 NSAID molar ratio of the original $[\text{Ru}_2(\text{NSAID})_4]$ paddlewheel unit which carries four NSAIDs per

dimetallic core. The antitumor activities of both metallodrugs, RuIbp and RuNpx, were higher than those of the corresponding parent drugs, HIBp and HNPx, for all the three tested cell lines. The non-drug RuAc showed the lowest activity, thus demonstrating that the anticancer activity is not related to the diruthenium core alone. The comparative data suggest synergistic effects between the metal and the NSAID drug in the metallodrugs, in agreement with the reported studies about the antiproliferative effects of RuIbp and aqua-RuNpx on C6 rat glioma cells.¹⁶ Nevertheless, the effects of either the NSAIDs or their respective metallodrugs, when administered in their free forms in breast and prostate cells, as assayed by MTT, may be considered too low (even at the highest concentrations tested here, 200 $\mu\text{mol L}^{-1}$ ($\text{Ru}_2(\text{NSAID})$ s) and 800 $\mu\text{mol L}^{-1}$ (free NSAIDs)) to be practically useful in anticancer therapy. The poor solubility in the culture medium, which will affect the intracellular bioavailability, might be one of the contributors to the low anticancer activity of the drugs in the tested cell lines. The encapsulation of the $\text{Ru}_2(\text{NSAID})$ metallodrugs or the NSAIDs into the SPLNs leads to a significant increase in the anticancer efficacy. Interestingly, the drug dose required for 50% cell growth inhibition (IC_{50}) values (Table 2) of the $\text{Ru}_2(\text{NSAID})$ -SPLNs (60–100 $\mu\text{mol L}^{-1}$ metallodrug) were in the acceptable range while the NSAID-SPLNs showed much higher values which were close to the experimental concentration limit. Therefore, even considering the NSAID-SPLNs at four-fold NSAID molar concentration in relation to the corresponding $\text{Ru}_2(\text{NSAID})$ -SPLNs, the anti-

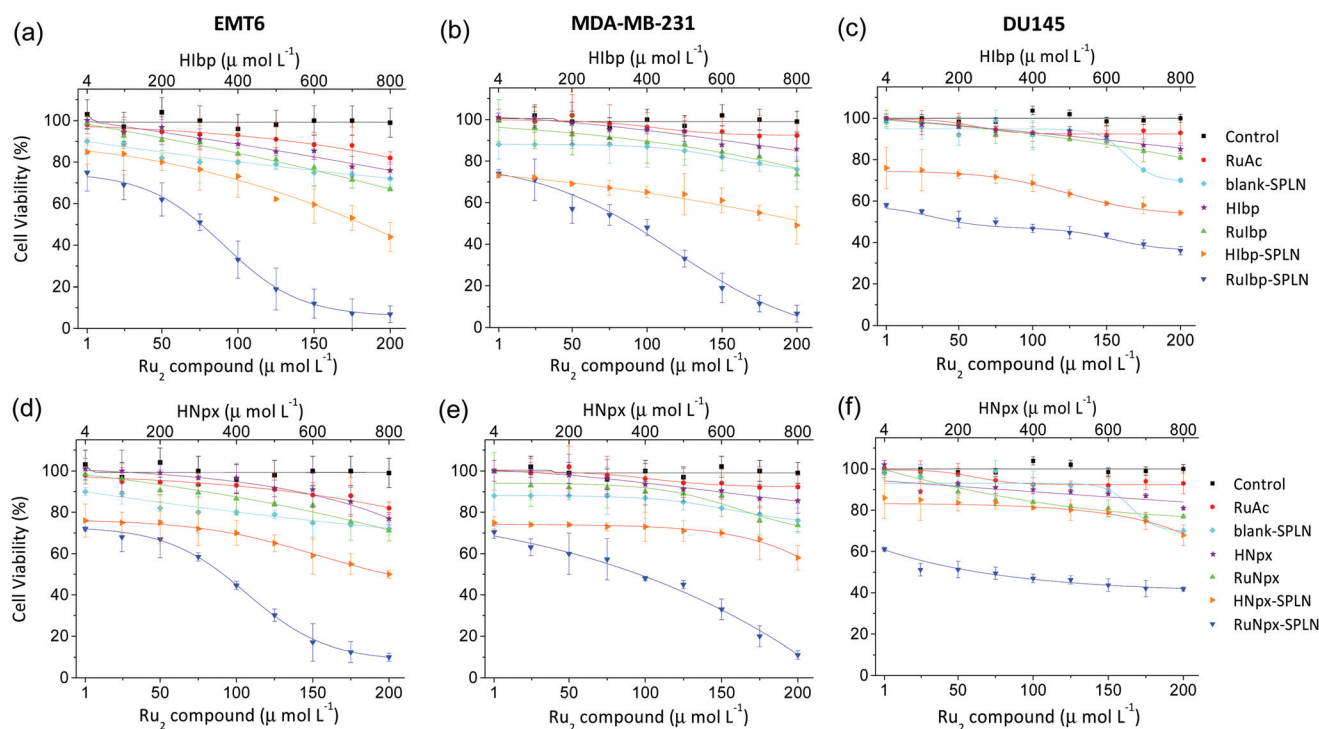


Fig. 6 Cell viability curves (MTT) at 48 h for (a) EMT6, (b) MDA-MB-231, and (c) DU145 treated with ruthenium compounds, ibuprofen and the corresponding SPLNs; (d) EMT6, (e) MDA-MB-231, and (f) DU145 treated with ruthenium compounds, naproxen and the corresponding SPLNs. Data are presented as mean \pm standard deviation ($n = 3$).

Table 2 IC₅₀ values of Ru₂(NSAID)-SPLNs. Data are presented as mean ± standard deviation (*n* = 3)

Cell line	IC ₅₀ (μmol L ⁻¹)	
	RuIbp-SPLNs	RuNpx-SPLNs
EMT6	67.0 ± 7.7	95.6 ± 10.8
MDA-MB-231	70.3 ± 8.1	101.8 ± 6.7

p < 0.05

tumor activities of the metallodrug-SPLNs were much higher than those of the corresponding NSAID-SPLNs in all cell lines. This finding corroborates the proposal that synergistic effects between the metal and NSAID might contribute to the anti-tumor activity of the metallodrugs. Apparently, the Ru₂(NSAID)-SPLN formulations developed here may promote enhanced activity by carrying the metallodrugs into the cancer cells also in the form of distinct diruthenium-NSAID-My mixed species. The response of the two different types of breast cancer cell lines, *i.e.*, the EMT6 (Fig. 6a and d) and the MDA-MB-231 (Fig. 6b and e), to the Ru₂(NSAID)-SPLNs is dose-dependent in the range 1–200 μmol L⁻¹ metallodrug. The IC₅₀ values (Table 2) found for the different cell lines are not statistically significant (*p* > 0.05) for each drug formulation (RuNpx-SPLNs or RuIbp-SPLNs). Additionally, although the apparent behavior of the RuIbp-SPLNs and RuNpx-SPLNs is similar in all cell lines, the IC₅₀ values for the distinct NSAID-metallodrug formulations are statistically different. The RuIbp-SPLNs seems to be more cytotoxic than the RuNpx-SPLNs formulation. This finding suggests that the anticancer activity might depend on the type of metallodrug species in the nanoformulation possibly associated with the nature of the NSAID ligand.

Comparatively, the cell viability in the prostate DU145 cancer cells was lower than those in both breast cancer cells, after the treatment with the Ru₂(NSAID)-SPLNs at similar administered doses. The values of IC₅₀ could not be determined for the prostate cancer cells because despite these cells being sensitive at low doses of NPs, the shape of the cell viability curves indicated a dose-independent response in the range 1–200 μmol L⁻¹ metallodrug (Fig. 6c and f). The distinct metallodrug dose-response behaviors in the DU145 cells compared to the breast cancer cells might be associated with a mode of action possibly involving distinct COX expressions by these cell lines. It is known that the DU145 cell line does not express COX-2,⁶² while slightly expresses COX-1.^{62,63} RuIbp was previously found to not cause significant changes in the expression of COX-2, and to be effective in cell lines which do not express COX-2.^{16,17,20} In glioma cell lines, however, the mRNA COX-1 expression and protein levels were significantly increased after exposure to RuIbp.^{17,18} In addition, the DU145 cell line overexpresses microsomal prostaglandin E₂ synthase-1 (MPGES-1) and PGEs,⁶² which might be inhibited by RuIbp as suggested in previous studies with glioma.¹⁶ Nevertheless, the Ru₂(NSAID)-SPLN nanoformulations were shown to contain drug-myristate mixed species besides the pure Ru₂(NSAID) drug. Underlying mechanisms of cytotoxicity of the

Ru₂(NSAID)-SPLNs in breast and prostate cancer cells are topics of future studies.

3.5. *In vivo* and *ex vivo* biodistribution and tumor accumulation of SPLN

Fig. 7a shows the fluorescence images of the whole mouse bearing murine EMT6 breast tumor at different time points after *i.v.* injection of fluorescence-labeled SPLNs. Rapidly following the NPs injection, the fluorescence intensity increased throughout the mouse body while, shortly after, the accumulation of NPs was observed in the tumor and also in other body organs, including the bladder area. The fluorescence signal in the bladder area may suggest renal elimination of the NPs. The significant decrease of the fluorescence signal from 1 to 24 h in the whole body, excluding the tumor area, gives evidence for the longer tumor retention time of SPLNs. The tumor accumulation of SPLNs was also confirmed through the *ex vivo* fluorescence images of body tissues. Fig. 7b shows optical images of *ex vivo* organs and tumor at 4 and 24 h. Similar to *in vivo* imaging, in the *ex vivo* assays the fluorescence intensity in lungs, liver, heart, intestine and kidneys was higher at 4 h than at 24 h. A drastic decrease of fluorescence in organs was observed from 4 to 24 h. In contrast, the tumor fluorescence intensity remained at the same level up to 24 h, as observed during the *in vivo* fluorescence imaging. The fluorescence intensity in different body organs and tumor was quantified as an average radiant efficiency using the Xenogen IVIS software, and the data represented in unit area (for all organs and tumor) are shown in Fig. 7c. It is important to mention that the higher fluorescence in lungs is not related to a higher accumulation of NPs in this organ, since the lung volume is small compared to the tumor volume (see the size and NPs accumulation in lungs and tumor in Fig. 7a, after 24 h *i.v.* injection). The quantification of fluorescence images also confirmed the fast clearance of SPLNs from different body organs. A higher fluorescence signal in lungs and liver during the first few hours suggests the early redistribution of NPs from the vascular space. The high fluorescence in intestine at 4 h indicates that the first elimination route for NPs is possibly through the hepatobiliary system – feces pathway.⁶⁴ Although this is not a common route of NPs elimination following their *i.v.* administration, several NP formulations have been reported to interact with hepatocytes in the liver and pass to small intestine through the biliary tree.⁶⁵ Conversely, the high fluorescence in kidneys at 24 h post injection suggests NPs clearance mainly through the renal route. The percentage of NPs retained in different organs and tumor tissue was determined from 4 to 24 h post NPs injection. Fig. 7d shows the SPLNs retention in different tissues. In relation to the tumor tissue, a very fast clearance of NPs was found for the other body organs, including the lungs which were found to have a considerable amount of NPs at the first 4 h. The retention of the NPs at the tumor site is corroborated by the presence of almost 75% SPLNs in the tumor after 24 h. The higher NPs retention in the tumor might be associated with the EPR effect, arising from the defective tumor vascula-

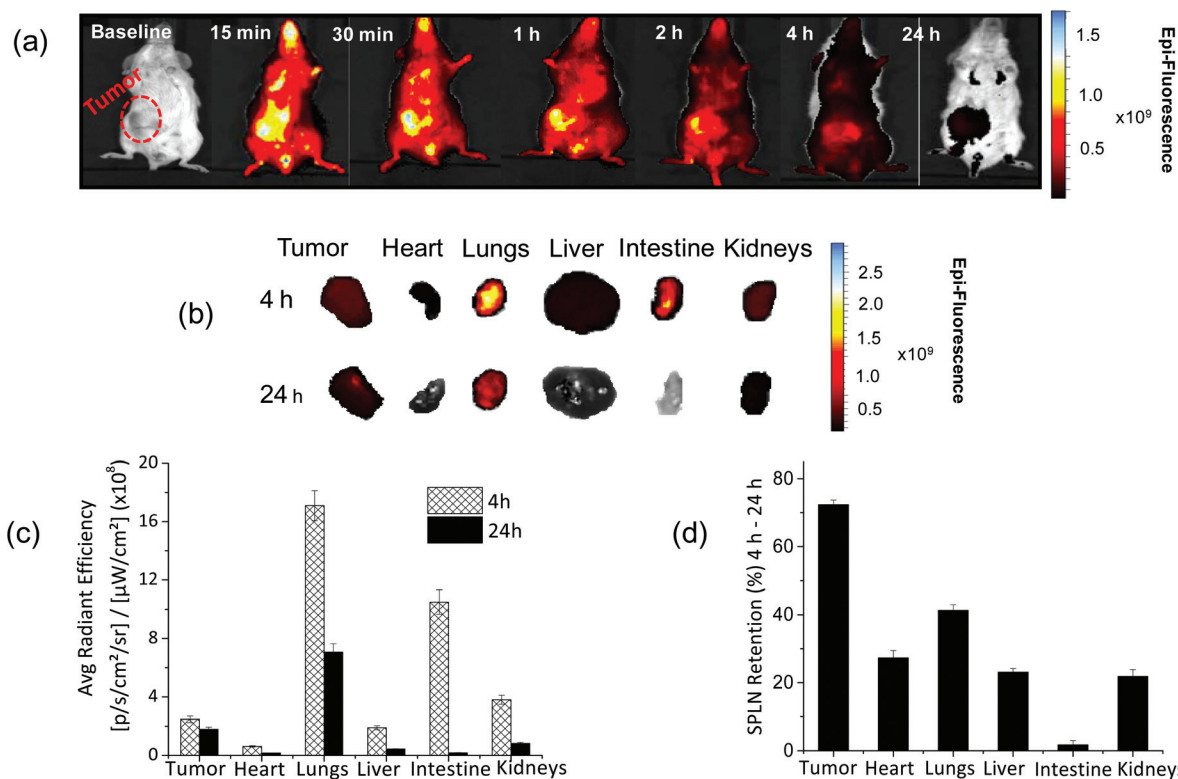


Fig. 7 *In vivo* biodistribution of ICG labeled SPLNs (a) and *ex vivo* studies to determine the distribution of SPLNs (b) in a BALB/c mouse bearing EMT6 breast tumor; average fluorescence intensity for each tissue at 4 and 24 h (c); retention of nanoparticles in percentage of fluorescence for each tissue (d). Data are presented as mean \pm standard deviation ($n = 3$).

ture and lymphatic drainage which may facilitate accumulation of the SPLNs in the tumor for extended times.⁶⁶

4. Conclusions

Novel nanoformulations containing diruthenium(II,III) metallo-drugs of ibuprofen or naproxen encapsulated into intravenously injectable solid-polymer-lipid nanoparticles (Ru₂(NSAID)-SPLNs) were successfully prepared from a rationally selected combination of two lipids (myristic acid and ethyl arachidate ester). The drug loading and the encapsulating efficiency were both high. The NPs were approximately spherical in shape, showing suitable values for particle size and zeta potential and good colloidal stability in serum at body temperature. The Ru₂(NSAID)-SPLNs showed enhanced cytotoxicity compared to the corresponding Ru₂(NSAID) metallo-drugs in breast (EMT6 and MDA-MB-231) and prostate (DU145) cancer cells *in vitro*. Apparently, the SPLN formulations developed here could promote enhanced activity by carrying the metallo-drugs into the cancer cells in the form of different diruthenium-NSAID-My mixed species. Fluorescence-labeled SPLNs were taken up by the cancer cells in a time- and energy-dependent manner as analyzed by confocal microscopy and fluorescence spectrometry. *In vivo* and *ex vivo* fluorescence imaging revealed good biodistribution and high tumor

accumulation of fluorescence-labeled SPLNs following *i.v.* injection in an orthotopic breast tumor model. The stability of the colloidal nanoparticles (suitable for *i.v.* injection) and their cellular uptake might be the major advantages to the enhanced anticancer activity for the metallo-drug-loaded SPLNs. These results broaden the perspectives of using Ru₂(NSAID) compounds to treat non-glioma tumors, such as breast and prostate cancer with high incidences affecting a large population of women and men. The findings of this work encourage future *in vivo* efficacy studies to further exploit the potential of the novel Ru₂(NSAID)-SPLN nanoformulations for clinical application.

Acknowledgements

The authors gratefully acknowledge financial support from the Brazilian agencies Fundação de Amparo à Pesquisa do Estado de São Paulo [FAPESP, research grants to D. de Oliveira Silva (2011/06592-1 and 2014/23047-5), a PhD fellowship to S. R. A. Rico (2014/23481-7, BEPE 2015/24252-4)], Conselho Nacional de Desenvolvimento Científico e Tecnológico [CNPq, a productivity fellowship to D. de Oliveira Silva (305914/2015-4), a PhD fellowship to G. Ribeiro], Coordenação de Aperfeiçoamento de Pessoal de Nível Superior [CAPES], Connaught International Scholarship for Doctoral Students by University of Toronto to T. Ahmed, and

Discovery and Equipment grants from the Natural Sciences and Engineering Research Council of Canada to X. Y. Wu. We thank the help from Dalva L. Faria (Raman) and Claudia R. Gordijo.

References

- S. Dhar and S. J. Lippard, Current status and mechanism of action of platinum-based anticancer drugs, in *Bioinorganic Medicinal Chemistry*, Wiley-VCH Verlag GmbH & Co. KGaA, Weinheim, Germany, 2011.
- X. Wang and Z. Guo, *Chem. Soc. Rev.*, 2013, **42**, 202–224.
- H. S. Oberoi, N. V. Nukolova, A. V. Kabanov and T. K. Bronich, *Adv. Drug Delivery Rev.*, 2013, **65**, 1667–1685.
- D. de Oliveira Silva, *Anti-Cancer Agents Med. Chem.*, 2010, 312–323.
- D. de Oliveira Silva, Ruthenium Compounds Targeting Cancer Therapy, in *Frontiers in Anti-cancer Drug Discovery*, ed. Atta-ur-Rahman and M. I. Choudhary, Bentham Science Publishers, Sharjah, U.A.E., 2014, vol. 4.
- S. J. Dougan and P. J. Sadler, *Chimia*, 2007, **61**, 704–715.
- A. Bergamo, C. Gaiddon, J. H. M. Schellens, J. H. Beijnen and J. G. Sava, *Inorg. Biochem.*, 2012, **106**, 90–99.
- B. S. Murraya, M. V. Babak, C. G. Hartinger and P. J. Dyson, *Coord. Chem. Rev.*, 2016, **306**, 86–114.
- E. Alessio, G. Mestroni, A. Bergamo and G. Sava, *Curr. Top. Med. Chem.*, 2004, **4**, 1525–1535.
- A. Bergamo and G. Sava, *Chem. Soc. Rev.*, 2015, **44**, 8818–8835.
- C. G. Hartinger, S. Zorbas-Seifried, M. A. Jakupec, B. Kynast, H. Zorbas and B. K. Keppler, *J. Inorg. Biochem.*, 2006, **100**, 891–904.
- R. Trondl, P. Heffeter, C. R. Kowol, M. A. Jakupec, W. Bergerbd and B. K. Keppler, *Chem. Sci.*, 2014, **5**, 2925–2932.
- G. Ribeiro, M. Benadiba, D. de O. Silva and A. Colquhoun, *Cell Biochem. Funct.*, 2010, 15–23.
- J. A. Miyake, M. Benadiba, G. Ribeiro, D. De Oliveira Silva and A. Colquhoun, *Anticancer Res.*, 2014, **34**, 1901–1912.
- A. Andrade, S. F. Namora, R. G. Woisky, G. Wiesel, R. Najjar, J. A. A. Sertié and D. de Oliveira Silva, *J. Inorg. Biochem.*, 2000, **81**, 23–27.
- G. Ribeiro, M. Benadiba, A. Colquhoun and D. de Oliveira Silva, *Polyhedron*, 2008, **27**, 1131–1137.
- M. Benadiba, R. R. P. dos Santos, D. De Oliveira Silva and A. Colquhoun, *J. Inorg. Biochem.*, 2010, **104**, 928–935.
- M. Benadiba, I. de M Costa, R. L. S. R. Santos, F. O. Serachi, D. de Oliveira Silva and A. Colquhoun, *J. Biol. Inorg. Chem.*, 2014, **19**, 1025–1035.
- Hanif-Ur-Rehman, T. E. Freitas, R. N. Gomes, A. Colquhoun and D. de Oliveira Silva, *J. Inorg. Biochem.*, 2016, **165**, 181–191.
- R. L. S. R. Santos, A. Bergamo, G. Sava and D. De Oliveira Silva, *Polyhedron*, 2012, **42**, 175–181.
- M. J. Thun, S. J. Henley and C. Patrono, *J. Natl. Cancer Inst.*, 2002, **94**, 252–266.
- R. E. Harris, R. T. Chlebowski, R. D. Jackson, D. J. Frid, J. L. Ascenseo, G. Anderson, A. Loar, R. J. Rodabough, E. White and A. McTiernan, *Cancer Res.*, 2003, **63**, 6096–6101.
- E. Gurpinar, W. E. Grizzle and G. A. Piazza, *Clin. Cancer Res.*, 2014, **20**, 1104–1113.
- C. N. Banti and S. K. Hadjikakou, *Eur. J. Inorg. Chem.*, 2016, 3048–3071.
- K. R. Dunbar, J. H. Matonic, V. P. Saharan, C. A. Crawford and G. Christou, *J. Am. Chem. Soc.*, 1994, **116**, 2201–2202.
- H. T. Chifotides and K. R. Dunbar, *Acc. Chem. Res.*, 2005, **38**, 146–156.
- R. L. S. R. Santos, R. Van Eldik and D. De Oliveira Silva, *Inorg. Chem.*, 2012, **51**, 6615–6625.
- R. L. S. R. Santos, R. van Eldik and D. de Oliveira Silva, *Dalton Trans.*, 2013, **42**, 16796–16805.
- M. Messori, T. Marzo, R. N. F. Sanches, Hanif-Ur-Rehman, D. de O. Silva and A. Merlino, *Angew. Chem., Int. Ed.*, 2014, **53**, 6172–6175.
- R. L. S. R. Santos, R. N. F. Sanches and D. de Oliveira Silva, *J. Coord. Chem.*, 2015, **68**, 3209–3228.
- H. L. Wong, R. Bendayan, A. M. Rauth, Y. Li and X. Y. Wu, *Adv. Drug Delivery Rev.*, 2007, **59**, 491–504.
- X. Y. Wu, *Expert Opin. Drug Delivery*, 2016, **13**, 609–612.
- R. X. Zhang, T. Ahmed, L. Y. Li, J. Li, A. Z. Abbasi and X. Y. Wu, *Nanoscale*, 2017, **9**, 1334–1355.
- H. L. Wong, R. Bendayan, A. M. Rauth and X. Y. Wu, *J. Controlled Release*, 2006, **116**, 275–284.
- A. J. Shuhendler, R. Staruch, W. Oakden, C. R. Gordijo, A. M. Rauth, G. J. Stanisz, R. Chopra and X. Y. Wu, *J. Controlled Release*, 2012, **157**, 478–484.
- C. R. Gordijo, A. Z. Abbasi, M. A. Amini, H. Y. Lip, A. Maeda, P. Cai, P. J. O'Brien, R. S. Dacosta, A. M. Rauth and X. Y. Wu, *Adv. Funct. Mater.*, 2015, **25**, 1858–1872.
- A. Z. Abbasi, P. Prasad, P. Cai, C. He, W. D. Foltz, M. A. Amini, C. R. Gordijo, A. M. Rauth and X. Y. Wu, *J. Controlled Release*, 2015, **209**, 186–196.
- A. J. Shuhendler, P. Prasad, H. C. Chan, C. R. Gordijo, B. Soroushian, M. Kolios, K. Yu, P. J. O. Brien, A. M. Rauth and X. Y. Wu, *ACS Nano*, 2011, **5**, 1958–1966.
- E. J. Henderson, A. J. Shuhendler, P. Prasad, V. Baumann, F. Maier-Flaig, D. O. Faulkner, U. Lemmer, X. Y. Wu and G. A. Ozin, *Small*, 2011, **7**, 2507–2516.
- A. J. Shuhendler, P. Prasad, M. Leung, A. M. Rauth, R. S. Dacosta and X. Y. Wu, *Adv. Healthcare Mater.*, 2012, **1**, 600–608.
- D. Shan, J. Li, P. Cai, P. Prasad, F. Liu, A. M. Rauth and X. Y. Wu, *Drug Delivery Transl. Res.*, 2014, **5**, 15–26.
- E. Blanco, H. Shen and M. Ferrari, *Nat. Biotechnol.*, 2015, **33**, 941–951.
- P. Prasad, A. Shuhendler, P. Cai, A. M. Rauth and X. Y. Wu, *Cancer Lett.*, 2013, **334**, 263–273.
- A. J. Shuhendler, P. Prasad, R. X. Zhang, M. A. Amini, M. Sun, P. P. Liu, R. G. Bristow, A. M. Rauth and X. Y. Wu, *Mol. Pharm.*, 2014, **11**, 2659–2674.

- 45 R. X. Zhang, P. Cai, T. Zhang, K. Chen, J. Li, J. Cheng, K. S. Pang, H. A. Adissu, A. M. Rauth and X. Y. Wu, *Nanomed. Nanotech. Biol. Med.*, 2016, **12**, 1279–1290.
- 46 T. Zhang, P. Prasad, P. Cai, C. He, M. Shan, A. M. Rauth and X. Y. Wu, *Acta Pharmacol. Sin.*, 2017, 1–13.
- 47 H. L. Wong, A. M. Rauth, R. Bendayan, J. L. Manias, M. Ramaswamy, Z. Liu, S. Z. Erhan and X. Y. Wu, *Pharm. Res.*, 2006, **23**, 1574–1585.
- 48 A. J. Shuhendler, R. Y. Cheung, J. Manias, A. Connor, A. M. Rauth and X. Y. Wu, *Breast Cancer Res. Treat.*, 2010, **119**, 255–269.
- 49 P. Prasad, J. Cheng, A. Shuhendler, A. M. Rauth and X. Y. Wu, *Drug Delivery Transl. Res.*, 2012, **2**, 95–105.
- 50 P. Heffeter, A. Riabtseva, Y. Senkiv, C. R. Kowol, W. Korner, U. Jungwith, N. Mitina, B. K. Keppler, T. Konstantinova, I. Yanchuk, R. Stoika, A. Zaichenko and W. Berger, *J. Biomed. Nanotechnol.*, 2014, **10**, 877–884.
- 51 W. J. Geary, *Coord. Chem. Rev.*, 1971, **7**, 81–122.
- 52 F. A. Cotton, C. Murillo and R. Walton, *Multiple Bonds Between Metal Atoms*, Springer Science & Business Media, New York, 3rd edn, 2005.
- 53 M. A. S. Aquino, *Coord. Chem. Rev.*, 1998, **170**, 141–202.
- 54 J. G. Norman, G. E. Renzoni and D. A. Case, *J. Am. Chem. Soc.*, 1979, **101**, 5256–5267.
- 55 V. Miskowski, T. Loehr and H. Gray, *Inorg. Chem.*, 1987, **26**, 1098–1108.
- 56 T. L. Moore, L. Rodriguez-Lorenzo, V. Hirsch, S. Balog, D. Urban, C. Jud, B. Rothen-Rutishauser, M. Lattuada and A. Petri-Fink, *Chem. Soc. Rev.*, 2015, **44**, 6287–6305.
- 57 X. Wen and E. Franses, *J. Colloid Interface Sci.*, 2000, **231**, 42–51.
- 58 R. Silverstein, G. Bassler and T. Morrill, *Spectroscopic Identification of Organic Compounds*, John Wiley and Sons, New York, 4th edn, 1981.
- 59 A. Arnould, A. A. Perez, C. Gaillard, J. P. Douliez, F. Cousin, L. G. Santiago, T. Zemb, M. Anton and A. L. Fameau, *J. Colloid Interface Sci.*, 2015, **445**, 285–293.
- 60 F. D. Cukiernik, M. Ibn-Elhaj, Z. D. Chaia, J.-C. Marchon, A.-M. Giroud-Godquin, D. Guillon, A. Skoulios and P. Maldivi, *Chem. Mater.*, 1998, **10**, 83–91.
- 61 S. Vranic, N. Boggetto, V. Contremoulins, S. Mornet, N. Reinhardt, F. Marano, A. Baeza-Squiban and S. Boland, *Part. Fibre Toxicol.*, 2013, **10**, 2–16.
- 62 H. Hanaka, S.-C. Pawelzik, J. I. Johnsen, M. Rakonjac, K. Terawaki, A. Rasmuson, B. Sveinbjörnsson, M. C. Schumacher, M. Hamberg, B. Samuelsson, P.-J. Jakobsson, P. Kogner and O. Rådmark, *Proc. Natl. Acad. Sci. U. S. A.*, 2009, **106**, 18757–18762.
- 63 V. Subbarayan, a. L. Sabichi, N. Llansa, S. M. Lippman and D. G. Menter, *Cancer Res.*, 2001, **61**, 2720–2726.
- 64 B. Zhao, L. Sun, W. Zhang, Y. Wang, J. Zhu, X. Zhu, L. Yang, C. Li, Z. Zhang and Y. Zhang, *Nanomed. Nanotech. Biol. Med.*, 2014, **10**, 839–849.
- 65 Y. N. Zhang, W. Poon, A. J. Tavares, I. D. McGilvray and W. C. W. Chan, *J. Controlled Release*, 2016, **240**, 332–348.
- 66 A. Schroeder, D. a. Heller, M. M. Winslow, J. E. Dahlman, G. W. Pratt, R. Langer, T. Jacks and D. G. Anderson, *Nat. Rev. Cancer*, 2011, **12**, 39–50.